Elastic properties and stress-temperature phase diagrams of high-temperature phases with low-temperature lattice instabilities

John C. Thomas and Anton Van der Ven

Elastic properties and stress-temperature phase diagrams of high-temperature phases with low-temperature lattice instabilities

John C. Thomas[*] and Anton Van der Ven[†]

Materials Department, University of California, Santa Barbara, California 93106, USA

The crystal structures of many technologically important high-temperature phases are predicted to have lattice instabilities at low temperature, making their thermodynamic and mechanical properties inaccessible to standard first principles approaches that rely on the (quasi) harmonic approximation. Here, we use the recently developed anharmonic potential cluster expansion within Monte Carlo simulations to predict the effect of temperature and anisotropic stress on the elastic properties of ZrH_2, a material that undergoes diffusionless transitions among cubic, tetragonal, and orthorhombic phases. Our analysis shows that the mechanical properties of high-temperature phases with low-temperature vibrational instabilities are very sensitive to temperature and stress state. These findings have important implications for materials characterization and multi-scale simulations and suggest opportunities for enhanced strain engineering of high-temperature phases exhibiting soft-mode instabilities.

I. INTRODUCTION

Despite posing theoretical challenges, strongly anharmonic crystals and high-temperature phases are found not only in naturally-occurring extreme environments, such as deep within Earth,[1] but also in many modern technological applications. Certain superconducting cuprates,[2] ferroelectric perovskites,[3] magnetic shape memory alloys,[4,5] and numerous transition metals, including Ti, Zr, and Hf, along with their hydrides[6] and oxides,[7] all exhibit high-symmetry phases at elevated temperature that density functional theory (DFT) predicts to be dynamically unstable at 0 K.

Transition metals and their alloys, in particular, are utilized extensively in extreme environments, where they may eventually coexist – and interact mechanically – with their hydrided and oxidized corrosion products. ZrH_{2-x}, for example, is an important corrosion product that precipitates within the Zr-alloy cladding of nuclear fuel rods. It has a complex phase diagram with a high-temperature cubic phase that, according to DFT, is mechanically unstable at 0 K with respect to tetragonal distortions.[6]

Constitutive relations for high-temperature phases are essential for predicting the behavior of engineering materials in extreme environments. However, the low-temperature lattice instabilities of cubic ZrH_2 and many other high-temperature phases make them particularly challenging for first principles simulation. It is common to approximate the elastic moduli of a particular crystal by its zero Kelvin values as determined by first-principles calculations of the curvature of the crystal potential energy with respect to strain. This approach fails for high-temperature phases that become mechanically unstable at low temperature as their 0-K potential energy surfaces become non-convex.

Common statistical mechanical approaches to calculate free energies at finite temperature such as the (quasi)-harmonic approximation are also inadequate for anharmonically-stabilized phases,[8–10] The prediction of constitutive relations for these materials instead requires models that rigorously treat anharmonic vibrational excitations. However, efficient and generalizable methods for studying finite-temperature anharmonic effects from first principles have remained elusive. *Ab initio* molecular dynamics, while accurate, cannot reach thermodynamic scales; self-consistent phonon theories, which describe the high-temperature phase using an approximate quasi-harmonic potential,[11,12] can estimate free energies but cannot be used near second-order transitions; effective Hamiltonians,[13–15] which use a reduced set of microscopic variables in order to describe anharmonicity of dynamically unstable degrees of freedom, can elucidate qualitative phenomena at the structural phase transition but are less suited to predicting accurate free energies or constitutive relations.

We recently developed a new formalism to construct arbitrarily improvable anharmonic Hamiltonians that are invariant to all symmetries of free space (i.e., rigid-body rotation and translation of coordinate system) as well as all space group symmetries of the high-symmetry reference crystal that becomes stable at elevated temperatures.[16] We demonstrated the ability of this method to predict the cubic to tetragonal second-order structural transition of unstressed ZrH_2. Monte Carlo simulations applied to the anharmonic Hamiltonian showed that cubic ZrH_2, which is mechanically unstable at zero Kelvin, is thermodynamically stabilized at high temperature by large-amplitude anharmonic vibrational excitations.[16]

Here we study the finite temperature mechanical properties of ZrH_2 using our recently developed first-principles anharmonic potential cluster expansion (APCE)[16] Hamiltonian within Monte Carlo simulations. We predict the elastic moduli of both the low-temperature tetragonal phase and the high-temperature cubic phase and find that they are very different. While cubic ZrH_2 is mechanically unstable at zero Kelvin, its

high-temperature elastic moduli show only a negligible dependence on temperature. The elastic moduli of the low temperature tetragonal form of ZrH_2, however, are highly anisotropic and exhibit surprisingly strong temperature dependence, indicating that anharmonic vibrational contributions to the mechanical properties of phases that undergo a second-order structural transition can be important. We also examine the effect of anisotropic stress states on elevated temperature elastic moduli and phase stability. Such anisotropic-stress boundary conditions are typical when a hydride such as ZrH_2 coexists coherently with its parent Zr metal.

II. METHODS

Measurements of the high-temperature phase of H-rich ZrH_x indicate that it has a cubic fluorite crystal structure consisting of a FCC Zr sublattice with H atoms at its tetrahedral sites.[17] Upon cooling, the crystal undergoes a symmetry-breaking diffusionless transformation to a tetragonal phase, with H remaining at tetrahedral sites of the FCT sublattice. The resulting crystal has one lattice parameter (c) that is shorter than the other two ($a = b$), indicating "negative" tetragonality, since $c/a - 1 < 0$. The tetragonality becomes more negative at lower temperatures, and DFT predicts $c/a \approx 0.88$ for ZrH_2 at 0 K.

We can unambiguously describe the large range of lattice deformations that can be realized in ZrH_2 using the Green-Lagrange finite strain tensor $\mathbf{E} = \frac{1}{2}\left(\mathbf{F}^\top\mathbf{F} - \mathbf{I}\right)$. $\mathbf{I}$ is the 3×3 identity tensor, and $\mathbf{F}$ is the deformation gradient tensor, which for homogeneous deformations maps the lattice vectors from the reference state to the deformed state, so that $\mathbf{E} = \mathbf{0}$ for the cubic reference crystal. $\mathbf{E}$ is symmetric, and using Kelvin notation, we represent its independent components as the vector

$$\vec{E} = (E_{xx}, E_{yy}, E_{zz}, \sqrt{2}E_{yz}, \sqrt{2}E_{xz}, \sqrt{2}E_{xy}). \quad (1)$$

The 2nd Piola-Kirchhoff stress, $\vec{\sigma}^{(P)}$, is work-conjugate to $\vec{E}$, such that $\sigma_m^{(P)} = (\partial A/\partial E_m)/\mathcal{V}_0$, where $A(T, \vec{E})$ is the Helmholtz free energy and $\mathcal{V}_0$ is the volume of the reference crystal.

The strain state $\vec{E}^\star$ is a stationary point of the free energy $A(T, \vec{E})$ when the constitutive stress equation satisfies $\vec{\sigma}^{(P)}(T, \vec{E}^\star) \equiv \vec{0}$. When $\vec{E}^\star = \vec{0}$ is a stationary point (as it is for cubic ZrH_2, because it corresponds to the high-symmetry reference crystal) the free energy at small strains is often approximated by the harmonic expression

$$A(T, \vec{E}) \approx A(T, \vec{0}) + \frac{1}{2}\mathcal{V}_0\vec{E}^\top\mathbf{C}(T, \vec{0})\vec{E}. \quad (2)$$

The 6×6 Lagrangian stiffness tensor $C_{mn}(T, \vec{E}^\star) = (\partial^2 A/\partial E_m\partial E_n)/\mathcal{V}_0$ is the first non-zero derivative of the free energy at a stationary point. When all the eigen-
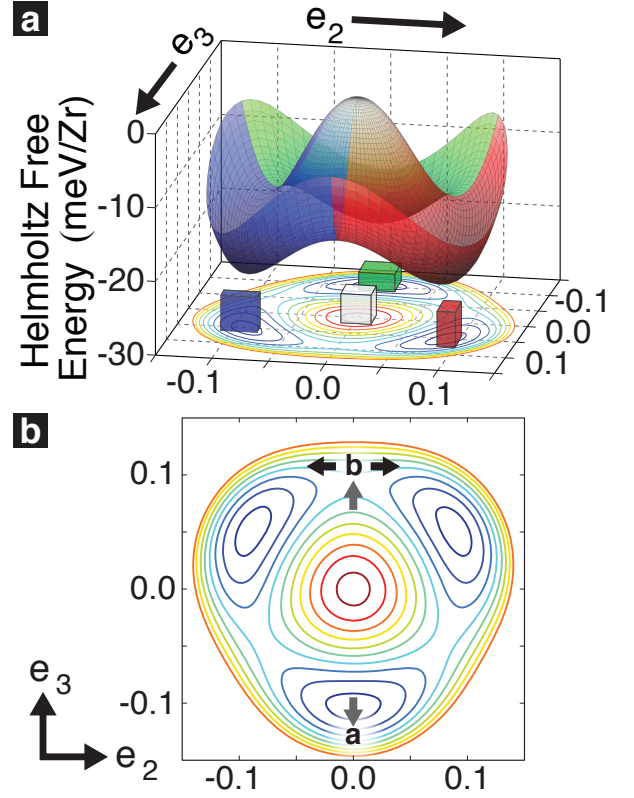

FIG. 1: (a) The 0-K potential energy surface of the ZrH_2 crystal in the e_2–e_3 plane, where colors indicate x (blue), y (red), and z (green) orientations of the negative tetragonal phase, with the three tetragonal strain orientations are illustrated pictorially. (b) A detail of the strain energy contours, where labeled point 'a' corresponds to a negative tetragonal deformation, which is convex, and labeled point 'b' corresponds to a positive tetragonal state, which is a saddle point.

values of $\mathbf{C}(T, \vec{E}^\star)$ are positive, the free energy is locally convex near $\vec{E}^\star$, and the stationary point is a minimum of the free energy.

It is possible to transform the vector $\vec{E}$ so that its components are aligned along 6 directions that preserve the most point-group symmetries, such that $\mathbf{C}(T, \vec{0})$ is always diagonal. One such basis is

$$e_1 = (E_1 + E_2 + E_3)/\sqrt{3}; \qquad e_4 = E_4;$$
$$e_2 = (E_1 - E_2)/\sqrt{2}; \qquad e_5 = E_5;$$
$$e_3 = (2E_3 - E_1 - E_2)/\sqrt{6}; \qquad e_6 = E_6,$$

which can be specified by the 6×6 matrix $\mathbf{Q}$ via $\vec{e} = \mathbf{Q}\vec{E}$. The e_i act as strain order parameters, where e_1 describes volumetric deformation, e_2 and e_3 describe deviatoric deformations (i.e., to tetragonal (I) and orthorhombic (F)), and e_4, e_5, and e_6 describe shear deformations (i.e., to rhombohedral, orthorhombic (I), and lower point symmetries). Because $\mathbf{Q}$ is an orthogonal matrix, the stress conjugate to $\vec{e}$ is simply the symmetry-adapted stress

$\vec{\Sigma}^{(P)} = \mathbf{Q}\vec{\sigma}^{(P)}$.

The strain order parameters e_2 and e_3 describe continuous paths linking cubic, tetragonal, and orthorhombic strains. When $e_2 = 0$, for example, e_3 describes z-oriented tetragonality, with $\text{sgn}(e_3) = \text{sgn}(c/a - 1)$. The 0-K Helmholtz free energy surface, shown in Fig. 1(a), has a local maximum at the origin of the e_2–e_3 subspace, corresponding to cubic ZrH_2, while local minima occur at negative tetragonal strains. The DFT-calculated stiffness tensor of cubic ZrH_2 thus has two negative eigenvalues, corresponding to e_2 and e_3, and the crystal is harmonically (or dynamically) unstable at $e_2 = e_3 = 0$. As such, the cubic crystal cannot exist as an equilibrium phase at low temperature, regardless of boundary conditions. Any small strain will spontaneously grow until reaching one of the three tetragonal minima. The positive tetragonal strains, opposite each negative tetragonal strain, are also dynamically unstable, and appear as saddle points in Fig. 1(a). These instabilities prevent us from describing the finite-temperature free energy of cubic ZrH_2 or predicting its constitutive relationships using a (quasi) harmonic phonon model.

Real materials often incorporate multiple coexisting phases, and hydrides can precipitate in Zr coherently or semi-coherently.[18,19] Mechanical equilibrium of a solid-state multi-phase coexistence induces tractions that impose a distinct anisotropic stress state on each individual phase. These boundary conditions deviate significantly from the usual hydrostatic boundary conditions and can significantly alter the phase stability of a precipitating hydride.[20] At fixed number of atoms N, anisotropic stress state $\vec{\sigma}^{(P)}$, and constant temperature T, the equilibrium state is determined by a minimum of the *anisotropic Gibbs potential*

$$\Phi = U - \mathcal{S}T - \mathcal{V}_0 \vec{E}^\top \vec{\sigma}^{(P)}, \qquad (3)$$

where $\mathcal{S}$ is entropy. Differentiation of Eq. (3) reveals that Φ is an explicit function of only T, $\vec{\sigma}^{(P)}$, and N, and that $E_i = -(\partial\Phi/\partial\sigma_i^{(P)})$.

The anharmonic potential cluster expansion formalism resolves many of the difficulties of studying high-temperature phases from first principles.[16] The APCE is a series expansion of the 0-K crystal potential energy surface in terms of multibody variables, called *cluster deformation amplitudes* (CDAs), which describe all deformational degrees of freedom of a cluster of two or more atoms. Because the CDAs are measured in the rotated frame of the deformed cluster, they are automatically invariant to rigid-body rotation and satisfy all symmetries of free space, making them ideal metrics for very large local deformations. The APCE basis functions are monomials of the CDAs that are invariant to the space group of ideal cubic ZrH_2.

The ZrH_2 APCE was fit to a set of 1484 crystal deformation energies calculated using DFT, as implemented in the Vienna ab-initio Simulation Package (VASP).[21–23] The DFT parameters and fitting procedure have been de-
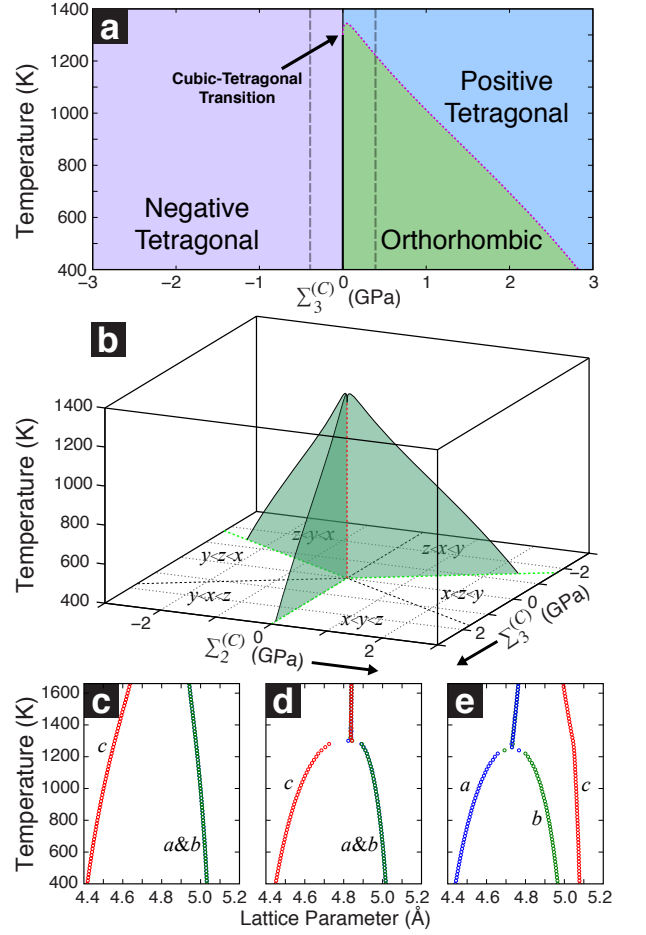

FIG. 2: The stress–temperature phase diagram for (a) the $\Sigma_2^{(C)} = 0$ contour and (b) the $(\Sigma_2^{(C)}, \Sigma_3^{(C)})$ plane; all other stress components are zero. Phases are characterized, in part, by the equilibrium lattice parameters, shown along iso-stress trajectories at (c) $\Sigma_2^{(C)} = 0$, $\Sigma_3^{(C)} = -392$ MPa; (d) $\Sigma_2^{(C)} = \Sigma_3^{(C)} = 0$; and (e) $\Sigma_2^{(C)} = 0$, $\Sigma_3^{(C)} = 392$ MPa; (c) and (e) correspond to thick dashed lines in (a).

scribed previously.[16] Because DFT calculations employ a variational approach to solve for the ground-state electronic structure, they do not account for the effect of electronic entropy. We explored the qualitative effect of electronic entropy in our previous work (Ref.[16]) and determined that electronic excitations should play a minor role compared to anharmonic vibrational excitations in determining thermodynamic properties. While electronic entropy may act to shift features of calculated properties to slightly lower temperatures, it should not qualitatively change the predictions presented here. The resulting APCE accurately describes the energetics of the 6 homogeneous strain components, as well as the $3N$ atomic coordinates, of the ZrH_2 crystal in terms of only 18 expansion coefficients.

We use the ZrH_2 APCE Hamiltonian to perform Metropolis MC simulations using a $N\vec{\sigma}^{(P)}T$ ensemble, in which homogeneous strains $\vec{E}$ and Zr displacement fields,
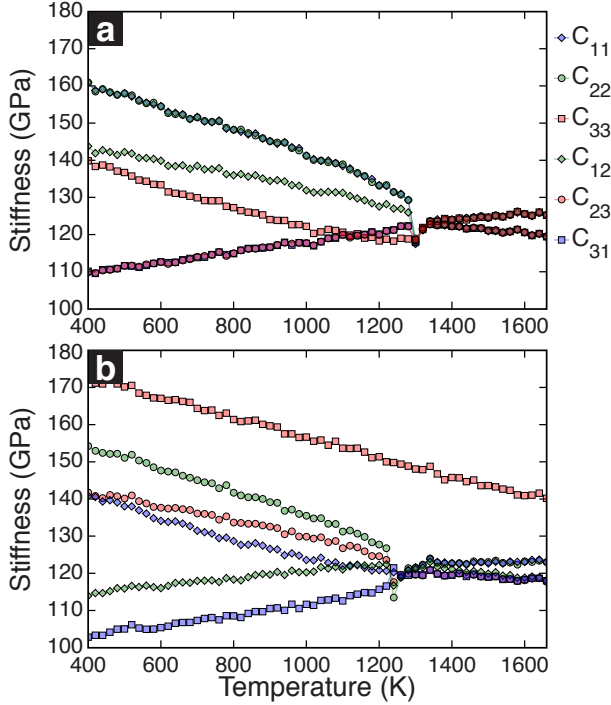
FIG. 3: Elements from the top left 3×3 block of the of the 6×6 stiffness tensor, calculated at (a) $\Sigma_2^{(C)} = \Sigma_3^{(C)} = 0$ MPa and (b) $\Sigma_2^{(C)} = 0$, $\Sigma_3^{(C)} = 392$ MPa. Shear stiffnesses (not shown) are comparatively soft and depend weakly on temperature and stress. C_{44}, C_{55}, and C_{66} range between 47-56 GPa at low temperature and converge toward 50 GPa at high temperatures; all other components are zero by symmetry. The stiffness components are indexed according to the same convention as the elements of $\vec{E}$ in Eq. (1).

specified by the $3N$-dimensional vector $\vec{R}$, were sampled according to the procedure described in Ref.[16]. Hydrogenic degrees of freedom can be factored out via a coarse-graining analysis.[16] Classically, the ensemble probability of a particular deformation state at constant stress is proportional to $\exp\left\{-\left[V(\vec{R}, \vec{E}) - \mathcal{V}_0 \vec{E}^\top \vec{\sigma}^{(P)}\right]/k_B T\right\}$, where $V(\vec{R}, \vec{E})$ is the APCE potential energy of the deformed crystal. Ensemble averaged quantities (e.g., $\langle E_i \rangle$) correspond to thermodynamic state variables that can be used to identify phase boundaries in temperature and stress space, from which we build the comprehensive ZrH$_2$ phase diagram.

Thermodynamic response functions, such as the Lagrangian compliance tensor, can be related to the ensemble-averaged covariance of the strain components, as can be shown by explicitly differentiating Φ in terms of the partition function to find

$$S_{ij} = -\frac{1}{\mathcal{V}_0} \frac{\partial^2 \Phi}{\partial \sigma_i^{(P)} \partial \sigma_j^{(P)}} = \frac{\mathcal{V}_0}{k_B T} \left(\langle E_i E_j \rangle - \langle E_i \rangle \langle E_j \rangle \right).$$

(4)

The Lagrangian stiffness tensor is given by $\mathbf{C} = \mathbf{S}^{-1}$. We report both $\mathbf{C}$ and $\mathbf{S}$ in Cartesian stress and strain coordinate systems (i.e., *not* the symmetry-adapted coordinates). However, we do perform a change of coordinates, using the average displacement gradient $\langle \mathbf{F} \rangle$ and volume $\langle \mathcal{V} \rangle$, so that the compliance tensor relates stresses and strains measured relative to the equilibrium lattice of the crystal (and not the reference cubic crystal). This change of coordinates allows easier comparison to typical experimental boundary conditions. All stresses reported here are Cauchy (or true) stresses (i.e., the stresses measured with respect to the equilibrium dimensions of the crystal). We denote the Cartesian Cauchy stresses as $\vec{\sigma}^{(C)}$ and the symmetry-adapted Cauchy stresses as $\Sigma_i^{(C)}$.

III. RESULTS

We performed Monte Carlo simulations within a $30 \times 30 \times 30$ supercell of the ZrH$_2$ primitive cell at temperature intervals of 20 K from 400 K to 1660 K, and at a number of anisotropic stress states in the $\Sigma_2^{(C)}$–$\Sigma_3^{(C)}$ space. The symmetry adapted stresses $\Sigma_2^{(C)}$ and $\Sigma_3^{(C)}$ are given explicitly by

$$\Sigma_2^{(C)} = \left(\sigma_1^{(C)} - \sigma_2^{(C)} \right)/\sqrt{2} \tag{5}$$

$$\Sigma_3^{(C)} = \left(2\sigma_3^{(C)} - \sigma_1^{(C)} - \sigma_2^{(C)} \right)/\sqrt{6}, \tag{6}$$

such that $\Sigma_2^{(C)} > 0$, $\Sigma_3^{(C)} = 0$ corresponds to pure shear stress in the x–y plane (i.e., tensile along x and compressive along y), and $\Sigma_2^{(C)} = 0$, $\Sigma_3^{(C)} > 0$ corresponds to isotropic compressive stress in the x–y plane and tensile stress along z. Thus, $\Sigma_3^{(C)}$ is a field that acts to make the crystal more tetragonal along z; $+120°$ off the $\Sigma_3^{(C)}$ axis in the $\Sigma_2^{(C)}$–$\Sigma_3^{(C)}$ plane describes a field that acts to make the crystal more tetragonal along y; and $-120°$ off the $\Sigma_3^{(C)}$ axis in the $\Sigma_2^{(C)}$–$\Sigma_3^{(C)}$ plane describes a field that acts to make the crystal more tetragonal along x. Thus, for ZrH$_2$, these three stresses are all symmetrically equivalent.

Simulations at various stress states along the $\Sigma_3^{(C)}$ axis were used to construct a ZrH$_2$ phase diagram in the $\Sigma_3^{(C)}$–T plane, shown in Fig. 2(a). The symmetries in the $\Sigma_2^{(C)}$–$\Sigma_3^{(C)}$ plane allow us to easily construct the three-dimensional ZrH$_2$ phase diagram, shown in Fig. 2(b). Clearly, small stresses can drastically change the phase stability of ZrH$_2$, as further evidenced by the equilibrium ZrH$_2$ lattice parameters, which are closely related to e_2 and e_3 and are shown in Figs. 2(c)–(e) for three different stress states along the $\Sigma_3^{(C)}$ axis.

Our simulations of unstressed ZrH$_2$ indicate that it undergoes a second-order cubic–tetragonal transition near 1300 K, in reasonable agreement with the T_c of 1200 K extrapolated from off-stoichiometric experimental measurements.[24] Under an applied negative tetrago-
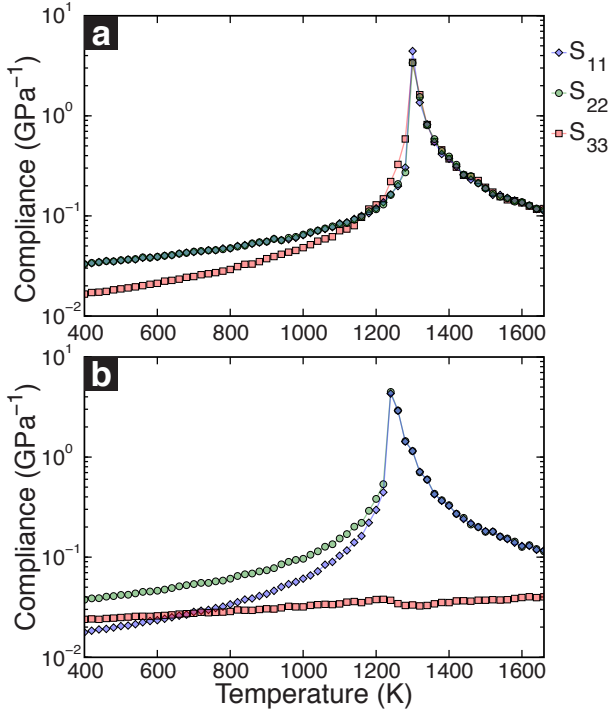
FIG. 4: The first three elements of the 6×6 compliance tensor, calculated at (a) $\Sigma_2^{(C)} = \Sigma_3^{(C)} = 0$ MPa and (b) $\Sigma_2^{(C)} = 0$, $\Sigma_3^{(C)} = 392$ MPa. (a) and (b) are plotted against semilog axes so that the divergence at T_c does not obscure low-temperature features. The compliance components are indexed according to the same convention as the elements of $\vec{E}$ in Eq. (1). The data were calculated in a $30 \times 30 \times 30$ supercell of the ZrH$_2$ primitive cell.

nal stress [Fig. 2(c)], the a and c lattice parameters become closer with temperature, but never meet, and thus the structural phase transition is completely suppressed. In contrast, the unstressed crystal [Fig. 2(d)], clearly becomes cubic near 1300 K.

More intriguingly, positive tetragonal stress yields an orthorhombic, rather than tetragonal, strain, and the crystal becomes tetragonal only above a stress-dependent T_c. Figure 2(e), shows the three distinct lattice parameters ($a < b < c$) under applied positive tetragonal stress at low temperature, which become tetragonal ($a = b < c$) near 1200 K. The reason for this symmetry-breaking phenomena can be illustrated using the 0-K free energy surface illustrated in Fig. 1(b). The point labeled 'a' in Fig. 1(b) is a deformation that can be realized at low temperature by imposing stress state with $\Sigma_2^{(C)} = 0$, $\Sigma_3^{(C)} < 0$ because the free energy has positive curvature at that point. By contrast, the point labeled 'b' in Fig. 1(b) is a positive tetragonal deformation, but it cannot be realized by applying a positive tetragonal stress at low temperature, because it is at a saddle point of the Helmholtz free energy. Instead, application of a positive tetragonal stress state will cause the crystal to fall into one of two equivalent orthorhombic deformation states,

which are indicated by the black arrows originating at point 'b' in Fig. 1(b). The arrows are oriented along e_2, which is the strain order parameter that describes the structural transition from the z-oriented tetragonal crystal to the orthorhombic crystal. As temperature rises, anharmonic excitations cause increasingly larger regions of the free energy to exhibit positive curvature, until the free energy of point 'b' finally becomes convex above T_c

Using Eq. 4, the APCE enables prediction of elastic properties over the entire stress-temperature phase space, even where the equilibrium strain is dynamically unstable at 0 K. Figures 3(a) and (b) show the calculated components from the upper 3×3 block of the 6×6 stiffness tensor, which describes the Cauchy stress induced by an infinitesimal strain. Our results reveal that anharmonic phase stabilization fundamentally alters the behavior of finite-temperature mechanical properties. At low temperatures, the calculated stiffness components of unstressed ZrH$_2$ [Fig. 3(a)] are similar to 0-K moduli of tetragonal ZrH$_2$ obtained from independent DFT analyses.[25] However, our results reveal the very strong thermoelastic response of unstressed ZrH$_2$ below T_c, where heating causes softening of all stiffness components except for C_{31} and C_{23}, which stiffen. Above T_c, the stiffness components, which now exhibit cubic symmetry, vary more weakly with temperature and are quite softer, on average, than their 0-K values. Pronounced critical softening of all stiffness components occurs at $T_c \approx 1300$ K, which is most visible as a divergence of the compliance components S_{11}, S_{22}, and S_{33}, which are shown for unstressed ZrH$_2$ in Fig. 4(a). The compliance components in Fig. 4(a) are shown on a logarithmic scale in order to reveal their temperature dependence away from T_c.

Application of anisotropic stress significantly changes the magnitude and temperature dependence of the elastic stiffness. The stiffness components at negative tetragonal stress (not shown) are slightly softer than in the unstressed state, and exhibit similar low-temperature trends, but because the phase transition is suppressed, no critical softening occurs. Under positive tetragonal stress, the 6 distinct stiffness components at low temperature [Fig. 3(b)] reflect the tetragonal–orthorhombic symmetry-breaking and differ significantly from the unstressed case. In particular, C_{31} and C_{12} become much softer under positive tetragonal stress, while C_{33} and C_{23} become much harder. The compliance components S_{11} and S_{22}, which are shown in Fig. 4(b), exhibit pronounced critical softening, in contrast to S_{33}, which remains continuous through the transition. The reason for this distinction is that, under the stress condition $\Sigma_3^{(C)} > 0$, $\Sigma_2^{(C)} = 0$, the orthorhombic–tetragonal order parameter is e_2, with $e_2 > 0$ indicating an orthorhombic crystal with $a_x < a_y$ and $e_2 < 0$ indicating an orthorhombic crystal with $a_y < a_x$, where a_x and a_y are the x- and y-aligned conventional lattice parameters, respectively. As such, S_{33} exhibits no divergence at the orthorhombic–tetragonal transition because E_3 is orthog-

onal to the order parameter e_2. Likewise, C_{13}, C_{33}, and C_{23} do not exhibit critical softening for the same reason.

IV.   DISCUSSION

Our analysis of ZrH_2 demonstrates how extreme anharmonicity, which exists when dynamically-unstable regions of the crystal potential energy surface are accessible at thermal energy scales, inevitably results in a complex interplay among stress, temperature, phase stability, and mechanical behavior. This is especially true when the dynamical instability is described by multiple order parameters, such as e_2 and e_3 for ZrH_2. Moreover, because the strain remains continuous through the structural transition, the lattice parameters deviate from their 0-K values even at low temperature due to strong anharmonic vibrational excitations. Consequently, the curvature of the 0-K energy surface does not accurately predict finite-temperature elastic properties, even below T_c. This extreme anharmonicity results in a strong temperature dependence of the moduli below T_c, as is evident in Figs. 3(a)-(b). We demonstrated that, by varying the direction and magnitude of stresses conjugate to the strain order parameters, we are able to either suppress the structural phase transition or qualitatively change its nature, which has practical importance for both application and mesoscale simulation.

Many high-temperature phases exist as polycrystals, whose domains typically experience symmetry-breaking stress boundary conditions. As we have shown here for the case of ZrH_2, such boundary conditions can significantly alter phase stability and mechanical properties. Experimentally, this distribution of stress states may result in apparent "smearing" of T_c and the associated critical phenomena. Theoretically, it significantly complicates predictive simulation of macroscopic systems. These difficulties are not readily apparent when using single crystals or powder samples for material characterization, and thus experimental data cannot necessarily resolve the unsuitability of 0-K calculations for parameterizing meaningful mesoscale and continuum models of anharmonically-stabilized phases.

The stochasticity of domain orientation in polycrystalline samples additionally complicates comparison of our results to experiment. The anisotropic mechanical properties of H-rich zirconium hydrides have not been characterized experimentally, although measurements of the Young's modulus and shear modulus have been performed on polycrystalline ZrH_x. Yamanaka, et al., calculated isotropic elastic moduli of polycrystalline ZrH_x pellets based on ultrasonic pulse–echo measurements of longitudinal and shear sound velocities at room temperature for x as high as 1.7[26]. They found that the elastic moduli decreased with the addition of hydrogen, and at $x \approx 1.7$ inferred a Young's modulus of 127 GPa and a shear modulus of 48 GPa. We can use the Voigt aver-

aging method[27] to approximate an upper bound on the elastic moduli of a polycrystal of ZrH_2 implied by our calculated stiffness tensor. The Voigt average gives the isotropic elastic properties of a textureless polycrystal of a harmonic solid under a homogeneous strain state. The Voigt-averaged Young's modulus, calculated from the stiffness tensor of the unstressed crystal [i.e., the values in Fig. 3(a)], is 99.9 GPa at 400 K and decreases with temperature until reaching a minimum of 83 GPa at cubic–tetragonal transition temperature. The Voigt-averaged shear modulus, again based on the data in Fig. 3(a), is 48.5 GPa at 400 K and decreases to a minimum value of 42.1 GPa at the T_c. The Voigt average is only a rough approximation of polycrystal elasticity, and the mechanical properties of a real polycrystal can depend strongly on microstructure and texture[28], especially for a strongly anharmonic material such as ZrH_2. Nevertheless, the Voigt-averaged moduli obtained from our calculations agree well with an extrapolation of the measurements reported by Yamanaka, et al.[26].

V.   CONCLUSION

We have predicted the elastic properties and high-temperature phase stability for anisotropic stress states of ZrH_2, a system exhibiting a high temperature cubic phase that becomes mechanically unstable at low temperature. Combining a first-principles anharmonic potential cluster expansion for ZrH_2 with Monte Carlo simulations we find a strong dependence of elastic moduli on both temperature and stress. Furthermore, phase stability and second-order transition temperatures are also found to be very sensitive to the anisotropic stress states typically found in solid-state multi-phase equilibrium. These results suggest that the mechanical properties of many important materials exhibiting high-temperature phases with low-temperature lattice instabilities cannot be estimated reliably with 0-K first-principles approaches or with measurements performed at room temperature under hydrostatic pressure conditions.

[*] Electronic address: johnct@engineering.ucsb.edu

[†] Electronic address: avdv@engineering.ucsb.edu

[1] S. Tateno, K. Hirose, Y. Ohishi, and Y. Tatsumi, Science **330**, 359 (2010).

[2] P. Böni, J. D. Axe, G. Shirane, R. J. Birgeneau, D. R. Gabbe, H. P. Jenssen, M. A. Kastner, C. J. Peters, P. J. Picone, and T. R. Thurston, Phys. Rev. B **38**, 185 (1988), URL http://link.aps.org/doi/10.1103/PhysRevB.38.185.

[3] P. Ghosez, E. Cockayne, U. V. Waghmare, and K. M. Rabe, Phys. Rev. B **60**, 836 (1999), URL http://link.aps.org/doi/10.1103/PhysRevB.60.836.

[4] P. J. Webster, K. R. A. Ziebeck, S. L. Town, and M. S. Peak, Philosophical Magazine Part B **49**, 295 (1984), http://dx.doi.org/10.1080/13642817408246515, URL http://dx.doi.org/10.1080/13642817408246515.

[5] M. Wuttig, J. Li, and C. Craciunescu, Scripta Materialia **44**, 2393 (2001), ISSN 1359-6462, URL http://www.sciencedirect.com/science/article/pii/S1359646201009393.

[6] R. Quijano, R. de Coss, and D. J. Singh, Phys. Rev. B **80**, 184103 (2009), URL http://link.aps.org/doi/10.1103/PhysRevB.80.184103.

[7] K. Parlinski, Z-.Q. Li, and Y. Kawazoe, Phys. Rev. Lett. **78**, 4063 (1997), URL http://link.aps.org/doi/10.1103/PhysRevLett.78.4063.

[8] P. J. Craievich, J. M. Sanchez, R. E. Watson, and M. Weinert, Phys. Rev. B **55**, 787 (1997), URL http://link.aps.org/doi/10.1103/PhysRevB.55.787.

[9] S. Baroni, S. de Gironcoli, A. Dal Corso, and P. Giannozzi, Rev. Mod. Phys. **73**, 515 (2001), URL http://link.aps.org/doi/10.1103/RevModPhys.73.515.

[10] G. Grimvall, B. Magyari-Köpe, V. Ozoliņš, and K. A. Persson, Rev. Mod. Phys. **84**, 945 (2012), URL http://link.aps.org/doi/10.1103/RevModPhys.84.945.

[11] P. Souvatzis, O. Eriksson, M. I. Katsnelson, and S. P. Rudin, Phys. Rev. Lett. **100**, 095901 (2008), URL http://link.aps.org/doi/10.1103/PhysRevLett.100.095901.

[12] O. Hellman, I. A. Abrikosov, and S. I. Simak, Phys. Rev. B **84**, 180301 (2011), URL http://link.aps.org/doi/10.1103/PhysRevB.84.180301.

[13] W. Zhong, D. Vanderbilt, and K. M. Rabe, Phys. Rev. Lett. **73**, 1861 (1994), URL http://link.aps.org/doi/10.1103/PhysRevLett.73.1861.

[14] W. Zhong, D. Vanderbilt, and K. M. Rabe, Phys. Rev. B **52**, 6301 (1995), URL http://link.aps.org/doi/10.1103/PhysRevB.52.6301.

[15] J. Bhattacharya and A. Van der Ven, Acta Materialia **56**, 4226 (2008), ISSN 1359-6454, URL http://www.sciencedirect.com/science/article/

[16] J. C. Thomas and A. Van der Ven, Phys. Rev. B **88**, 214111 (2013), URL http://link.aps.org/doi/10.1103/PhysRevB.88.214111.

[17] S. S. Sidhu, N. S. Satya Murthy, F. P. Campos, and D. D. Zauberis, *Neutron and X-Ray Diffraction Studies of Nonstoichiometric Metal Hydrides* (The American Chemical Society, Washington, DC, 1963), chap. 9, pp. 87–98, Advances in Chemistry Series No. 39, http://pubs.acs.org/doi/pdf/10.1021/ba-1964-0039.ch008, URL http://pubs.acs.org/doi/abs/10.1021/ba-1964-0039.ch008.

[18] G. Carpenter, Acta Metallurgica **26**, 1225 (1978), ISSN 0001-6160, URL http://www.sciencedirect.com/science/article/pii/0001616078900068.

[19] G. Weatherly, Acta Metallurgica **29**, 501 (1981), ISSN 0001-6160, URL http://www.sciencedirect.com/science/article/pii/0001616081900742.

[20] Q. Xu and A. Van der Ven, Phys. Rev. B **76**, 064207 (2007), URL http://link.aps.org/doi/10.1103/PhysRevB.76.064207.

[21] G. Kresse and J. Furthmüller, Phys. Rev. B **54**, 11169 (1996).

[22] G. Kresse and J. Furthmüller, Computational Materials Science **6**, 15 (1996), ISSN 0927-0256, URL http://www.sciencedirect.com/science/article/pii/0927025696000080.

[23] G. Kresse and D. Joubert, Phys. Rev. B **59**, 1758 (1999), URL http://link.aps.org/doi/10.1103/PhysRevB.59.1758.

[24] K. Moore and W. Young, Journal of Nuclear Materials **27**, 316 (1968), ISSN 0022-3115, URL http://www.sciencedirect.com/science/article/pii/0022311568900901.

[25] P. Olsson, A. Massih, J. Blomqvist, A.-M. A. Holston, and C. Bjerkén, Computational Materials Science **86**, 211 (2014), ISSN 0927-0256, URL http://www.sciencedirect.com/science/article/pii/S0927025614000615.

[26] S. Yamanaka, K. Yoshioka, M. Uno, M. Katsura, H. Anada, T. Matsuda, and S. Kobayashi, Journal of Alloys and Compounds **293295**, 23 (1999), ISSN 0925-8388, URL http://www.sciencedirect.com/science/article/pii/S0925838899003898.

[27] R. Cook and W. Young, *Advanced Mechanics of Materials* (Macmillan, London, 1985).

[28] J. Den Toonder, J. Van Dommelen, and F. Baaijens, Modelling and Simulation in Materials Science and Engineering **7**, 909 (1999).